Received: 25 January 2021 | Revised: 26 June 2021 | Accepted: 6 July 2021

DOI: 10.1002/hbm.25595

RESEARCH ARTICLE

WILEY

Relating quantitative 7T MRI across cortical depths to cytoarchitectonics, gene expression and connectomics

Peter McColgan[1,2] | Saskia Helbling[1] | Lenka Vaculčiaková[1] | Kerrin Pine[1] | Konrad Wagstyl[3] | Fakhereh Movahedian Attar[1] | Luke Edwards[1] | Marina Papoutsi[2] | Yongbin Wei[4] | Martijn Pieter Van den Heuvel[4] | Sarah J Tabrizi[2] | Geraint Rees[3] | Nikolaus Weiskopf[1,5]

[1]Department of Neurophysics, Max Planck Institute for Human Cognitive and Brain Sciences, Leipzig, Germany

[2]Huntington's Disease Research Centre, Institute of Neurology, University College London, London

[3]The Wellcome Centre for Human Neuroimaging, Institute of Neurology, University College London, London, UK

[4]Vrije Universiteit Amsterdam, Complex Traits Genetics Lab, Amsterdam, Netherlands

[5]Felix Bloch Institute for Solid State Physics, Faculty of Physics and Earth Sciences, Leipzig University, Leipzig, Germany

Correspondence
Peter McColgan, Department of Neurophysics, Huntington's Disease Centre, UCL Institute of Neurology, 2nd Floor Russell Square House, 10-12 Russell Square,London.
Email: p.mccolgan@ucl.ac.uk

Funding information
Bundesministerium für Bildung und Forschung, Grant/Award Number: 01EW1711A & B; FP7 Ideas: European Research Council, Grant/Award Number: 616905; Scientific Education and Research Institute, Grant/Award Number: 15.0137; Swiss State Secretariat for Education, Research and Innovation (SERI); European Union's Horizon 2020 research and innovation programme, Grant/Award Number: 681094

Abstract

Ultra-high field MRI across the depth of the cortex has the potential to provide anatomically precise biomarkers and mechanistic insights into neurodegenerative disease like Huntington's disease that show layer-selective vulnerability. Here we compare multi-parametric mapping (MPM) measures across cortical depths for a 7T 500 μm whole brain acquisition to (a) layer-specific cell measures from the von Economo histology atlas, (b) layer-specific gene expression, using the Allen Human Brain atlas and (c) white matter connections using high-fidelity diffusion tractography, at a 1.3 mm isotropic voxel resolution, from a 300mT/m Connectom MRI system. We show that R2*, but not R1, across cortical depths is highly correlated with layer-specific cell number and layer-specific gene expression. R1- and R2*-weighted connectivity strength of cortico-striatal and intra-hemispheric cortical white matter connections was highly correlated with grey matter R1 and R2* across cortical depths. Limitations of the layer-specific relationships demonstrated are at least in part related to the high cross-correlations of von Economo atlas cell counts and layer-specific gene expression across cortical layers. These findings demonstrate the potential and limitations of combining 7T MPMs, gene expression and white matter connections to provide an anatomically precise framework for tracking neurodegenerative disease.

KEYWORDS
gene expression, histology, neurodegeneration, ultra-high field MRI

1 | INTRODUCTION

The advent of ultra-high field (UHF) MRI now enables us to image the human brain at sub-millimetre resolution in vivo. Combining this technological advance with quantitative MRI (qMRI) has made in-vivo histology MRI (hMRI) a distinct possibility (Trampel, Bazin, Pine, & Weiskopf, 2019; Weiskopf, Mohammadi, Lutti, & Callaghan, 2015). Multi-parametric maps (MPMs) include qMRI parameters of effective transverse relaxation rate (R2*), which are sensitive to both myelin and iron (Edwards, Kirilina, Mohammadi, & Weiskopf, 2018; Kirilina

et al., 2020; Weiskopf et al., 2013) and longitudinal relaxation rate (R1), which is mainly sensitive to myelin and to a lesser extent to iron (Stuber et al., 2014) (for review, see Weiskopf, Edwards, Helms, Mohammadi, & Kirilina, 2021).

The human neocortex is composed of six distinct cyto-architectonic cortical layers, which are defined based on cell density, cell size and cell type. In-vivo high-resolution histology using ultra-high field (UHF) qMRI has the potential to provide cortical layer-specific measures that relate to these patterns of cell composition and associated layer-specific gene expression. Previous studies using high-resolution qMRI showed myelination patterns across cortical areas but also assessed cortical profiles of qMRI parameters at 3T (Carey et al., 2018; Dick et al., 2012; Sereno, Lutti, Weiskopf, & Dick, 2013) and 7T (Cohen-Adad et al., 2012; Marques, Khabipova, & Gruetter, 2017; Sprooten et al., 2019). How qMRI measures across cortical depths relate to cytoarchitecture at different cortical layers however is largely unknown. Such layer-specific in-vivo histology could also enable us to investigate neurodegenerative disease with much greater anatomical precision. For example, in end-stage Huntington's disease post-mortem studies show involvement of layers 3, 5 and 6 (Rub et al., 2016), while in multiple sclerosis (MS) sub-pial cortical changes are seen particularly in secondary progressive MS (Derakhshan, Caramanos, Narayanan, Arnold, & Louis Collins, 2014; Tardif, Bedell, Eskildsen, Collins, & Pike, 2012). Thus, layer-specific in-vivo high-resolution qMRI has the potential to provide mechanistic insights into layer-selective vulnerability, as well as anatomically precise cortical biomarkers.

In this study, we aim to investigate the relationship between cortical depth measures using 7T qMRI in healthy humans in-vivo to established histological and gene expression measures. For this purpose, we relate R1 and R2* at different cortical depths from in-vivo high-resolution MPMs to post-mortem whole brain histology atlases, gene enrichment atlases and whole brain connectomics derived from diffusion MRI (dMRI). To this end, we acquired whole brain MPMs at 7T with 500 μm resolution and high-fidelity dMRI in a group of 10 healthy young adults.

We use the von Economo–Koskinas whole brain histology atlas to provide layer-specific quantitative cell measures. Von Economo and Koskinas parcellated the cerebral cortex into 56 regions based on cell type, cell size and cell count (C. F. K. von Economo & Koskinas, 1925). We could therefore test the hypothesis that qMRI parameters at different cortical layers would relate to cell measures in corresponding histology layers. Going beyond cell histology, the Allen Human Brain Atlas (AHBA) provides a densely sampled atlas of regional gene expression across the human brain (Hawrylycz et al., 2012). This allowed us to link qMRI parameters across cortical depths with layer-specific gene expression (Burt et al., 2018).

Prior to disease onset, Huntington's disease is characterised by striatal atrophy and a subsequent loss of cortico-striatal white matter (WM) connections (McColgan et al., 2015) formed by pyramidal tract neurons in layer 5. To demonstrate the relationship of UHF qMRI parameters to WM connections we relate qMRI across cortical depths to WM connections from high-fidelity dMRI.

Our results show significant correlations between R2* maps and post-mortem layer-specific cytoarchitecture and between R2* and gene expression pattern. Further, we demonstrate a strong relationship between WM connections and qMRI across cortical layers. Limitations of the layer-specific relationships demonstrated are at least in part related to the high cross-correlations of von Economo atlas cell counts and layer-specific gene expression across cortical layers. Our findings highlight the unique opportunities, as well as the limitations, provided by MR-based in-vivo histology to establish an anatomically precise framework that can be used to track neurodegenerative disease.

2 | MATERIALS AND METHODS

2.1 | Data acquisition

Data from 10 healthy volunteers (6 females, 4 males, mean age 28 ± 3.6 years) were acquired on a 7T whole-body MRI system (Magnetom 7T, Siemens Healthineers, Erlangen, Germany) equipped with a 1-channel transmit/32-channel radio-frequency (RF) receive head coil (Nova Medical, Wilmington, MA). The MPM protocol consisted of two multi-echo fast low angle shot (FLASH) scans with T1- and PD-weighting (T1w, PDw), plus maps of the radio frequency (RF) transmit field $B1^{+}$ and static magnetic field B0. The MPM acquisition was adapted for whole-brain coverage at 500 μm isotropic resolution from methods described previously (Kirilina et al., 2020; Lutti, Dick, Sereno, & Weiskopf, 2014; Trampel et al., 2019; Weiskopf et al., 2011; Weiskopf et al., 2013).

The PD-weighted and T1-weighted multi-echo FLASH scans were acquired with flip angles of 5° and 24 ° respectively, readouts of alternating polarity to give 6 echoes evenly spaced between 2.8 and 16 ms, and a TR of 25 ms for a total imaging time of 18 min per volume. Additional parameters were as follows: matrix size (read × phase × partition) 496 × 434 × 352, sagittal orientation, generalised autocalibrating partial parallel acquisition (GRAPPA) (Griswold et al., 2002) with acceleration factor 2 in both phase and partition directions (inner phase encoding loop), non-selective excitation with a sinc-shaped RF pulse, readout bandwidth 420 Hz/pixel. The transmit voltage was calibrated by an initial low-resolution transmit field map to be optimal over the occipital lobe. Motion was monitored and corrected prospectively by an optical tracking system (Kineticor, Honolulu, HI) (Callaghan et al., 2015). For the purposes of prospective motion correction of the high resolution MPM acquisitions, each volunteer was scanned while wearing a mouth guard assembly (with attached passive Moiré pattern markers) moulded to their front teeth (manufactured by the Department of Cardiology, Endodontology and Periodontology, University Medical Center Leipzig; (Papoutsi et al., 2018)). R1, R2* and PD parameter maps were computed using the hMRI toolbox (Tabelow et al., 2019).

Diffusion weighted images (DWI) were acquired for the same participants on a 3T Connectom (Siemens Healthineers, Erlangen, Germany) scanner (300 mT/m maximum gradient strength) using a 32-channel RF head coil for reception and a body RF coil for transmission. DWI were

acquired with high isotropic spatial resolution (voxel size = 1.3 × 1.3 × 1.3 mm^3) and four interleaved diffusion weighting shells (b = 500 s/mm^2, b = 1,000 s/mm^2, b = 2,000 s/mm^2, b = 3,000 s/mm^2) to enable simultaneous partial volume effect (PVE) and crossing fibre modelling of the underlying voxel-wise fibre populations (Jeurissen, Tournier, Dhollander, Connelly, & Sijbers, 2014). DWI were acquired along 24, 36, 60 and 60 non-collinear diffusion encoding directions in the order of lowest to highest b-value shell. The diffusion encoding was achieved using monopolar diffusion weighting gradients and the diffusion weighting directions were distributed on the whole-sphere for optimum balancing and eddy current (EC)-induced distortion correction (Andersson & Sotiropoulos, 2016). A total of 24 non-DWI (b = 0 s/mm^2) were also acquired as baseline signal at every ten DWI ($b \neq 0$ s/mm^2) intervals. A Centre for Magnetic Resonance Research (CMRR) sequence was used for the DWI acquisition. This was a single-shot, two-dimensional, multi-slice spin-echo echo planar imaging (SE-EPI) sequence (flip angle 90°, TE = 65.60 ms, TR = 5,500 ms, partial Fourier factor = 5/8, in-plane acceleration factor in phase encoding (PE) direction (GRAPPA) = 2 (Griswold et al., 2002). A multi-band acceleration factor (in slice direction) of 2 was used (CMRR, University of Minnesota, Minneapolis, MN. https://www.cmrr.umn.edu/multiband/, (Feinberg et al., 2010; Moeller et al., 2010; Setsompop et al., 2012; Xu et al., 2013). The acquisition included leak-block kernel reconstruction, readout bandwidth = 1,234 Hz/Px, effective PE bandwidth = 13.256 Hz/Px, echo spacing = 0.93 ms, acquisition matrix = 210 × 212.5 (101.2% FOV phase), reconstructed matrix = 162 × 164, number of axial slices = 90, distance factor = 0% and frequency selective fat suppression with both saturation RF pulses and the principle of slice selection gradient reversal (Nagy & Weiskopf, 2008). The DWI were acquired with phase encoding (PE) in the anterior–posterior (AP) direction. The DWI acquisition was repeated twice to improve the signal-to-noise ratio (SNR). Five additional non-DWI (b = 0 s/mm^2) were acquired at the beginning of the DWI sequence preceded by the acquisition of five non-DWI (b = 0 s/mm^2) with reversed PE gradient polarity, that is, posterior–anterior (PA) instead of anterior–posterior (AP) encoding direction. The collection of AP-PA non-DWI (b = 0 s/mm^2) enabled correction of susceptibility-induced geometric distortions in the DWI (Andersson & Sotiropoulos, 2016). The total DWI acquisition time was approximately 50 min.

An accompanying 3D magnetization-prepared rapid gradient-echo (MPRAGE) image was acquired in the same session as the diffusion MRI with the following imaging parameters: voxel size = 1 × 1 × 1 mm^3, TR/TE = 2,300/2.91 ms, flip angle = 9°, parallel acceleration factor (GRAPPA) = 2, field-of-view = 256 and 240 mm, matrix size = 256 × 240 × 176, sagittal slices acquired with AP phase encoding, non-selective inversion recovery with inversion time TI = 900 ms, fat suppression and RF spoiling.

2.2 | Cortical layer construction

To enable surface-based registration of cortical atlases to individual subjects the FreeSurfer Version 6.0 recon-all pipeline was used (Fischl et al., 2004) for cortical surface reconstruction. As the pipeline is designed for standard T1w MPRAGE images the following modifications were made for the 7T MPMs. A synthetic FLASH volume with optimal white matter/grey matter contrast was created using the FreeSurfer mri_synthesize routine with TR = 20 ms, flip angle = 30°, TE = 2.5 ms. Inputs to the routine were scaled quantitative PD and T1 maps (1/R1 volumes, with removal of a small number of negative and extremely high values produced by estimation errors). SPM segment (https://www.fil.ion.ucl.ac.uk/spm) was applied to the synthetic image to create a combined grey matter (GM)/white matter (WM)/cerebrospinal fluid (CSF) brain mask with a tissue probability cut-off of 0, which was used to remove the skull from the PD image. The PD image (normalised such that the average white matter intensity is at 69% (Tabelow et al., 2019)) was then subtracted from 100%, inverting the contrast and thus making it more MPRAGE-like. Next, Rician denoising (http://www.cs.tut.fi/~foi/GCF-BM3D) (Maggioni, Katkovnik, Egiazarian, & Foi, 2013) was applied and the resulting image was used for FreeSurfer cortical surface reconstruction. This was preferable to using the 3T 1 mm isotropic T1w MPRAGE, which would have required registration to the 7T MPM images.

FreeSurfer was then used to perform surface-based registration of the von Economo (Scholtens, de Reus, de Lange, Schmidt, & van den Heuvel, 2018), HCP-MMP 1.0 (Glasser et al., 2016) and Desikan-Killiany (Desikan et al., 2006) atlases from template to subject space. The digital von Economo atlas was created by manual segmentation of individual T1 scans based on the cortical regions defined in the von Economo–Koskinas post mortem atlas (Scholtens et al., 2018). This enables direct ROI comparison of von Economo–Koskinas layer-specific cell measures with 7T MPM measures across cortical depths. The HCP-MMP 1.0 atlas was chosen for the genetic analysis as the finer grained resolution of 180 ROIs (compared to 43 ROIs for von Economo and 34 ROIs for Desikan-Killiany) enabled us to maximise the number of genetic data points sampled for the Allen Human Brain Atlas (AHBA). The Desikan-Killiany atlas was chosen for the connectome analysis as it contains both cortical and sub-cortical ROIs (as opposed to cortex only for HCP-MMP 1.0). The number of reconstructed streamlines required for reproducibility rises exponentially with larger parcellation schemes (Yeh, Smith, Liang, Calamante, & Connelly, 2018), thus we considered using the Desikan-Killiany atlas to be the optimal approach. With this caveat in mind, we repeated the connectome analysis using a combined HCP-MMP 1.0 cortical and subcortical aseg parcellation, produced from FreeSurfer recon-all pipeline, and have presented this in the Supporting Information. For all parcellation schemes, analyses were confined to the left hemisphere, except in the case of inter-hemispheric connections in the connectome analyses.

In order to create cortical layers, first CAT12 (http://www.neuro.uni-jena.de/cat) was used to create GM and WM tissue probability maps (TPMs) from the synthetic T1w image. In CAT12, the synthetic image was spatially normalised using an affine and a non-linear registration, bias field correction was applied and the image was segmented into GM, WM and CSF (Farokhian, Beheshti, Sone, & Matsuda, 2017). CAT12 was used instead of SPM segment as it resulted in more accurate WM segmentations for the 7T images with

much higher WM tissue probabilities. In order to construct conservative GM and WM masks, the GM and WM TPMs were thresholded such that values below 1 converted to 0. This was done in order to avoid erroneous labelling of GM as WM at the GM/WM boundary. The GM TPM was manually corrected to improve minor segmentation errors. Nighres (Huntenburg, Steele, & Bazin, 2018) was used to create level set images from the GM and WM masks. The resulting outer and inner level set images were used to create 8 equi-volume layers.

R1 and R2* were sampled at each layer creating profile-sampled images. These were masked using ROIs from the von Economo (Scholtens et al., 2018), HCP-MMP 1.0 (Glasser et al., 2016) and Desikan-Killiany (Desikan et al., 2006) atlases and mean R1 and R2* values were extracted for each ROI for each layer per participant. Values were then averaged across participants and only the left hemisphere was used in order to match the data from the AHBA, since it contains data from 6 left hemispheres and only 2 right hemispheres. Thus, this analysis was in keeping with previous analyses using only the left hemisphere (Arnatkevic Iute, Fulcher, & Fornito, 2019). This resulted in matrices of 8×43 for von Economo and 8×180 for HCP-MMP 1.0 atlases.

We also applied a surface-based pipeline using the FreeSurfer Version 6.0 recon-all pipeline. The Freesurfer pial and white matter surfaces were then used to create equi-volume cortical layers using surface tools (https://github.com/kwagstyl/surface_tools). However, on visual inspection the pial and GM/WM boundaries created using CAT12 were more accurate across the whole brain for our data.

2.3 | Diffusion MRI processing

A white matter connectome was created for each participant using anatomically constrained tractography (Smith, Tournier, Calamante, & Connelly, 2012) implemented in MRtrix (Tournier, Calamante, & Connelly, 2012). Raw diffusion images were first visually quality controlled. Denoising (Veraart et al., 2016) and Gibbs ringing artefact removal was performed (Kellner, Dhital, Kiselev, & Reisert, 2016) using MRtrix. FSL Eddy and Top-up were used to correct for eddy currents, susceptibility-related distortion and subject movement (Andersson & Sotiropoulos, 2016). Bias field correction was then performed using the ANTS N4 algorithm (Tustison et al., 2010). Voxel-wise fibre orientation distribution were calculated using multi-shell multi-tissue constrained spherical deconvolution (MSMT-CSD) (Jeurissen et al., 2014), with group averaged response functions for WM, GM and CSF. Intensity normalisation was then performed on fibre orientation distributions (FODs) and probabilistic whole brain tractography implemented to generate 10 million streamlines. Streamlines terminated when exiting the white matter. Spherical deconvolution informed filtering of tractograms (SIFT2) was used to remove biases inherent in tractography where longer connections are over-determined, streamlines follow the straightest path and lack an associated volume (Smith, Tournier, Calamante, & Connelly, 2013). FreeSurfer was used (Fischl et al., 2004) to segment and parcellate the whole brain 3T MPRAGE image. The resulting Desikan-Killiany (Desikan et al., 2006) and associated subcortical aseg parcellation, produced from FreeSurfer recon-all pipeline, was used to construct the WM connection matrix. R1 and R2* weighted connectomes were also created by taking the average R1/R2* value across streamlines connecting a pair of ROIs, where higher R1/R2* were used as indicators for a higher myelination and stronger connectivity. This is analogous to fractional anisotropy weighting of streamlines, which is commonly used in white matter connectome studies, but more directly targets the myelination of connections (van den Heuvel & Sporns, 2011). Cortico-striatal, cortico-thalamic, cortico-cortical, inter-hemispheric and intra-hemispheric connections were then extracted for each Desikan-Killiany ROI per subject and averaged across the group.

2.4 | Cell histology and genetic atlases

Cell count and cell size data across cortical layers for the von Economo atlas were taken from (C. von Economo, 2009), which provides cell count and cell size data for each cortical layer 1–6 in every von Economo atlas ROI. By translating the von Economo regions into comparable FreeSurfer Desikan-Killiany atlas regions (Scholtens, de Reus, & van den Heuvel, 2015) demonstrated highly significant correlation with post-mortem cortical thickness and in-vivo MRI cortical thickness. Subsequently the von Economo regions themselves have been mapped to MRI template space (Scholtens et al., 2018; van den Heuvel, Scholtens, & Kahn, 2019). This enabled us to directly test the sensitivity of UHF qMRI parameters to cytoarchitecture.

Layer-specific cell staining intensity measures from the Big Brain atlas were also used to examine cortical depth MPM measures, as a complementary layer-specific histology atlas to von Economo (these results are presented in the Supporting Information).

Gene expression data for the AHBA was extracted for 180 left-hemisphere regions of the HCP-MMP 1.0 atlas as detailed by (Arnatkevic Iute et al., 2019). Data was available from six neurotypical human brains (6 left hemispheres and 2 right hemispheres). Only data for the left hemisphere was used as the dataset for the right hemisphere was incomplete. Genetic data processing involved six steps: gene information re-annotation, data filtering, probe selection, sample assignment, data normalisation and gene filtering. The code to run these processing steps is available at https://github.com/BMHLab/AHBAprocessing. The processed data for 180 left-hemisphere regions of the HCP-MMP 1.0 atlas is available at https://doi.org/10.6084/m9.figshare.6852911. Lists of genes specific to cortical layers 2–6 were obtained from the supplementary information of Bernard et al. (2012). These lists are derived from Macaque layer-specific gene expression data from a range of cortical regions including the anterior cingulate, dorsolateral prefrontal cortex, orbitofrontal cortex, primary motor and somatosensory cortices, temporal area, hippocampus and primary auditory cortex. Rhesus macaque and humans have strong similarities in molecular architecture, making this a highly predictive nonhuman primate model system for human neocortical gene expression (Bernard et al., 2012).

2.5 | Experimental design and statistical analysis

For R1 and R2* pairwise Pearson correlations were performed at the ROI level (N = 43) and between each cortical depth and each von Economo cortical layer across 43 regions of the MRI template space von Economo atlas. This resulted in 8x6 (8 depths in MRI x 6 layers in von Economo) correlations for each quantitative map. A Bonferroni-corrected *p*(corrected) < .05 threshold was applied to correct for multiple comparisons (implemented by a *p*(uncorrected) < .05/(8 × 6)). Pearson correlation 95% confidence interval (CI) values are provided for analyses at the ROI level. The R2*, R1 and von Economo cell count analyses were repeated but excluding selected ROIs. To assess the possible effect of typical artefacts at 7T the frontal and temporal pole ROIs from the von Economo atlas were excluded. To assess the possibility that the observed relationships were driven by primary sensory areas the von Economo ROIs precentral area, agranular frontal area and striate area were excluded (see Supporting Information). Potential outlier ROIs were also investigated by taking the residuals from the linear fit for the R2*/R1 versus von Economo cell count analyses and plotting them for each ROI onto the FreeSurfer average inflated cortical surfaces (see Figure S12).

For the genetic analysis, R1 and R2* were each averaged for each layer within each HCP-MMP 1.0 ROI. A principal component analysis (PCA) was performed on gene expression data for layers 2, 3, 4, 5 and 6 separately to identify the dominant patterns of gene expression variation across HCP-MMP 1.0 ROIs. For each PCA the first principal component was selected, and Pearson correlations were performed between R1 and R2* at the ROI level (*N* = 180), respectively (Bonferroni-corrected *p* < .05/5). Correlations were also performed for mean gene expression for each gene list in order to confirm the direction of correlation from the PCA analysis. Across cortical depths Pearson correlations were performed between R2* and layer-specific genes creating a matrix of 8 depths × 5 layers (for each gene set) (Bonferroni-corrected *p* < .05/[8 × 5]). Cross-correlations for layer-specific genes were also examined and are presented in Supporting Information.

For the connectome analysis white matter connections were split into 5 groups (cortico-striatal, cortico-thalamic, cortico-cortical, inter-hemispheric or intra-hemispheric). Correlations were then performed between these white matter subtypes and MRI cortical depth across the 34 Desikan-Killiany atlas regions resulting in an 8 depths × 5 connection sub-type correlation matrix. Bonferroni correction was applied for multiple comparisons (Bonferroni-corrected *p* < .05/[8 × 5]). Streamlines were either multiplied by: (a) cross-sectional area (Smith, Tournier, Calamante, & Connelly, 2015) based on diffusion signal (streamline weighting), (b) average R1 (R1 weighting) or (c) average R2* (R2* weighting).

R2* analyses for von Economo, Big Brain, layer specific gene expression and the connectomics analysis were also performed at the single subject level. Similarly the R1 and R2* weighted connectome analyses were repeated for single subjects. These analyses are presented in Supporting Information (Figures S5–S9).

3 | RESULTS

3.1 | R2* and R1-based myelination patterns across cortical regions and depths

The first aim of this study was to use UHF qMRI to reproduce known myelination patterns across both primary sensory and association cortices. We expected that both effective transverse relaxation rate (R2*) and longitudinal relaxation rate (R1) would be higher in primary sensory areas, such as the primary visual cortex V1, than the rest of the cortex. To this aim, R2* and R1 were sampled at 50% equi-volume cortical depth and averaged across all participants. Visual inspection of R1 and R2* revealed high values in the motor and auditory cortices and in the primary visual area V1 (Figure 1) consistent with post-mortem histology and cortical myelination patterns reported for 3T T1-weighted/T2-weighted images (Glasser et al., 2016), 3T R1 maps (Sereno et al., 2013), 7T R1 maps (Haast, Ivanov, Formisano, & Uludag, 2016) and R2* maps (Marques et al., 2017).

R1 was highest for V1, consistent with previous T1w/T2w ratio maps and R1 maps at 3T. However, the middle temporal area (MT), which is reported as heavily myelinated at 3T, showed lower R1 values (Glasser et al., 2016; Sereno et al., 2013) compared to most other regions tested in the visual cortex. These patterns were generally consistent across depths (Figure 2a). For R2* both V1 and region MT values were greater nearest the pial surface, and then initially decreased in the middle depths before increasing between the middle and deep depths reaching highest values at the GM/WM boundary (Figure 2b).

Sensorimotor myelination patterns were consistent with patterns of T1w/T2w ratio maps at 3T and with post mortem histology (Geyer et al., 1996; Glasser et al., 2016; Hopf, 1968). Brodmann Area (BA) 3b showed higher R1 values than BA 3a, except for the two most superficial depths. BA 2 and BA 1 showed low values for both R1 and R2*, across all cortical depths. The values in the primary motor cortex, BA 4, were highest relative to other regions in the middle depths for both R1 and R2*. In BA 3a, R1 and R2* values decrease sharply between the superficial and middle depths (Figure 2c,d). In general, R2* tends to be higher in very superficial layers, which may be caused by susceptibility effects in pial surface veins containing paramagnetic deoxygenated haemoglobin (i.e., the blood oxygen level dependent [BOLD] effect).

For the auditory cortex R1 values for primary auditory cortex A1, para belt, posterior belt (PBelt) and medial belt (MBelt) were similar, while R2* showed better discrimination of these regions. For both R1 and R2* retroinsular cortex (RI) showed the lowest values relative to neighbouring regions. This is consistent with T1w/T2w patterns at 3T (Glasser et al., 2016). Sharp decreases in R2* were seen between the superficial and middle depths in particular for lateral belt (LBelt) and parabelt (PBelt). Again, this may be related to blood vessel artefacts at the pial surface causing higher values at the most superficial layers. With this exception, patterns were consistent with the literature across cortical depths for R2* and R1 (Figure 2e,f).

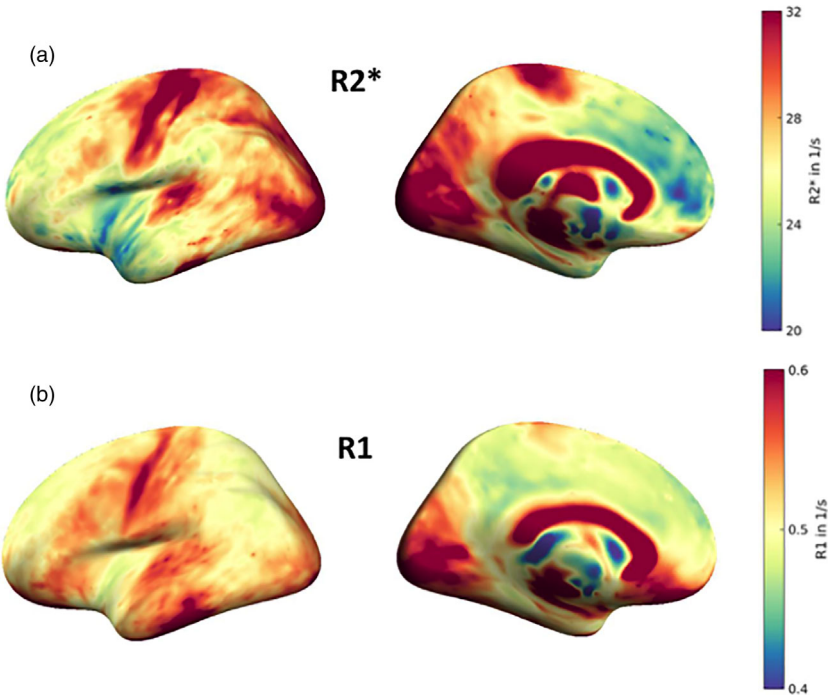

FIGURE 1 R2* and R1 values sampled at 50% cortical depth projected on FreeSurfer average inflated cortical surfaces (a) R2* (in 1/s) (b) R1 (in 1/s)

The superior parietal cortex was chosen as an example of a multimodal association area. Using T1w/T2w at 3T (Glasser et al., 2016) reported that MIP has less myelin than lateral intra-parietal dorsal cortex (LIPd) and lateral intra-parietal ventral cortex (LIPv), but MIP has more myelin than lateral parietal 7 area (7PL) and intra-parietal 1 (IP1) area. R2* values (Figure 3h) were most consistent with this showing higher MIP values compared with 7PL and IP1 across most cortical depths, with LIPd values higher than MIP in the superficial and middle depths. R1 values (Figure 2g) are less consistent as LIPd and LIPv are lower than MIP across most cortical depths.

In summary the R1 and R2* values we measured using 7T qMRI for sensory, motor and association cortices were generally consistent with known patterns of myelination, supporting their validity. Therefore, we proceeded to investigate their relationship to cytoarchitectonics, layer-specific gene expression and connectomics.

3.2 | R2* is highly correlated with von Economo cell count

To examine the sensitivity of the R1 and the R2* measures to cytoarchitectonic properties, we compared R1 and R2* at the ROI level and across cortical depths with von Economo cell count and cell size. Motivated by the relation between cyto- and myeloarchitecture and the myelin-sensitive quantitative MRI measures (Dinse et al., 2015; Hellwig, 1993), we hypothesised that UHF qMRI parameters across cortical depths would correlate with cell measures in post-mortem cortical layers, such R1 and R2* at depths near the pial surface would correlate with superficial layers, R1 and R2* at mid-depths would correlate with layer 4, while R1 and R2* at depths near the GM/WM boundary would show greater correlation with deep layers. However, we note that cells at a given layer will also affect qMRI values in layers below them, as qMRI measures are sensitive to myelin and iron, which are present in axon collaterals.

At the ROI level significant correlations were seen between R2* and von Economo cell count (rho $= 0.65$, $p = 2.93 \times 10^{-6}$, 95% CI 0.45–0.80) (Figure 3a). Across cortical layers Bonferroni corrected significant correlations for R2* were seen in von Economo layers 2 (across all R2* cortical depths), 3 (for mid cortical R2*, depths 3–6), 4 (across R2* cortical depths 1–7) and 6 (for R2* superficial layers, depths 2–3) (Figure 3b). Correlations for R2* were absent for von Economo layers 1 and 5. This is likely due to the small number of cells in layer 1 and the large size of pyramidal cells in layer 5 (C. von Economo, 2009).

For the R1 analysis, no Bonferroni-corrected significant correlations were seen at the ROI level for von Economo cell count (Figure 3c). Across layers no Bonferroni-corrected significant correlations were seen for the von Economo data (Figure 3d).

Correlations at between R2* and von Economo at the ROI level and across cortical depths remained similar both with the exclusion of ROIs prone to 7T artefact and primary sensory areas. Similar patterns between R1 and von Economo were also seen when these ROIs were excluded (see Figures S10 and S11).

Our findings show R2* but not R1 is highly correlated with cell count across cortical depths particularly for layers 2, 3, 4 and 6. The presence of high cross correlations of von Economo cell count between layers (see Figure S2) may at least partly account for the lack of layer specificity of the observed correlations between the MRI parameters and histological measures.

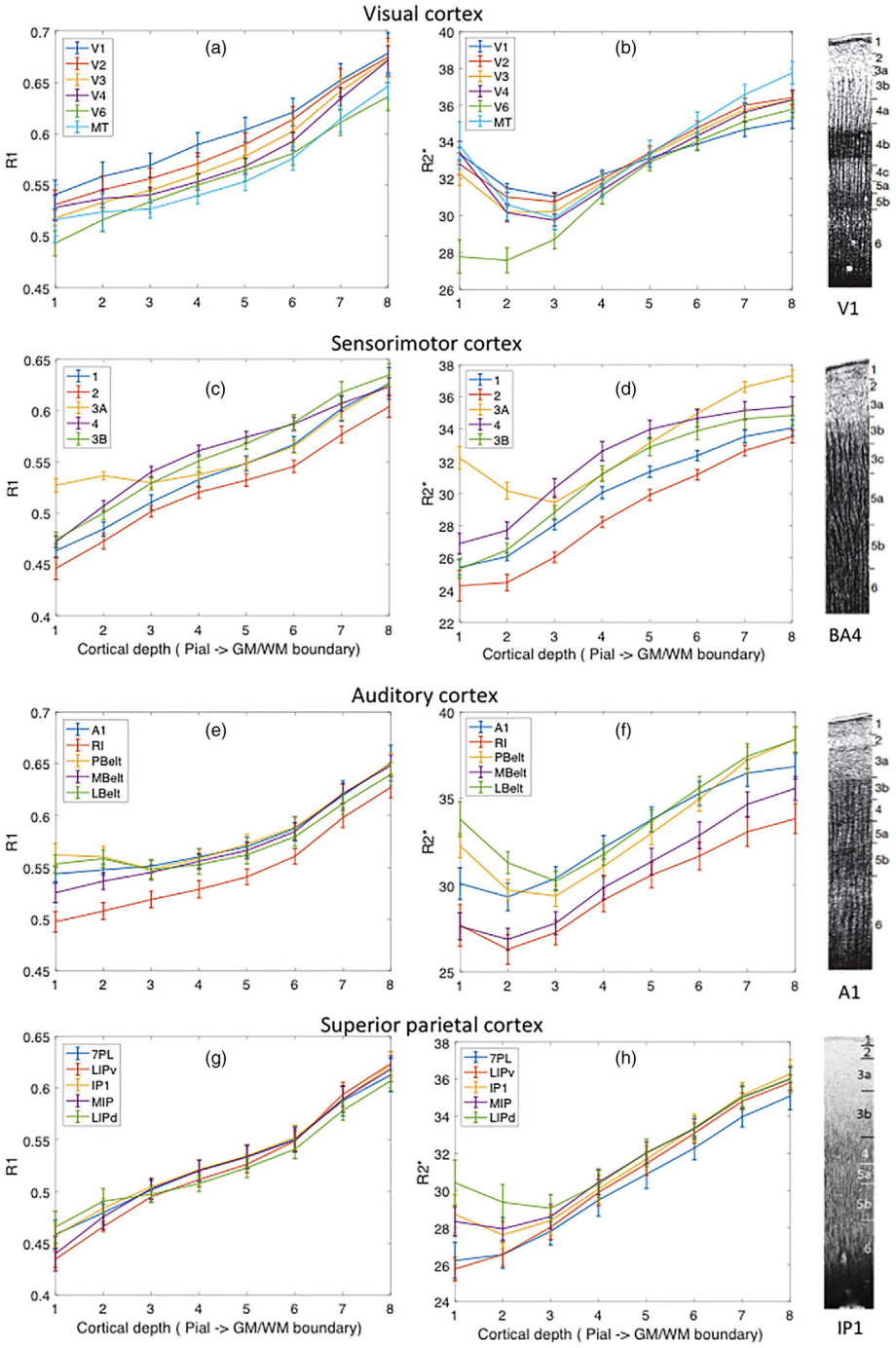

FIGURE 2 R1 and R2* profiles across primary sensory, primary motor and association cortices. Cortical depth profile, where *y*-axis is MRI contrast (R1 or R2*) and *x*-axis is equi-volume cortical depth (1—nearest pial surface, 8—nearest grey matter/white matter [GM/WM] boundary), for visual cortex (a) R1 and (b) R2*, sensorimotor motor cortex (c) R1 and (d) R2*, auditory cortex (e) R1 and (f) R2* and superior parietal cortex (g) R1 and (h) R2*. GM—grey matter, WM—white matter, V1—primary visual area, V2–V6—visual areas 2 to 6, MT—middle temporal area. 1—area 1, 2—area 2, 3a—area 3a, 3b—area 3b, 4—area 4 (primary motor cortex). A1—primary auditory cortex, RI—retroinsular cortex, MBelt—medial belt, LBelt—lateral belt, PBelt—parabelt. 7PL—lateral area 7P, LIPv—area lateral intra-parietal ventral, IP1—intra-parietal 1, MIP—medial intra-parietal area, LIPd—area lateral intra-parietal dorsal. Standard error of the mean (SEM) is displayed as error bars for each cortical depth. Cortical labels refer to Glasser et al. (2016). Myeloarchitectonic profiles presented alongside graphs are reproduced from Zilles, Palomero-Gallagher, and Amunts (2015) and based on original drawings by Vogt and Vogt (1919) were layers are defined based on myeloarchitectonics not equi-volume cortical layers. Profiles are provided for areas V1 (singulostriate—absence of inner Baillarger stripe), BA4 (astriate—Baillarger stripes cannot be delineated), A1 (unitostriate—both Baillarger stripes appear to be fused to a broad band) and IPL (bistriate—both Baillarger stripes are clearly detectable). These images are not included in the CC-BY 4.0 licence

3.3 | R2* is highly correlated with layer-specific genes

To further examine the relationship between qMRI parameters and layer-specific properties, we next investigated the relationship between R1 and R2* and layer-specific genes. In a similar vein to the cytoarchitectural features, we hypothesised qMRI parameters in depths near the pial surface would correlate with genes specific to layers 2 and 3, mid-depths would correlate with layer 4 and depths near the GM/WM boundary would correlate with layers 5 and 6. Again, we note that cells at a given layer may affect qMRI values in layers below them, as qMRI measures are sensitive to myelin and iron, which are present in axon collaterals.

Percentage of total variance explained for the first PCA component were as follows; layer 2–21%, layer 3–24%, layer 4–34%, layer 5–32% and layer 6–42%. Significant Bonferroni-corrected correlations were seen for R2* averaged across layers and ROI with genes specific to cortical layer 2 (rho $= -0.73$, $p = 2.24 \times 10^{-30}$, 95% CI −0.79 to −0.66), layer 3 (rho $= -0.78$, $p = 1.32 \times 10^{-36}$, 95% CI −0.83 to −0.71), layer 4 (rho $= 0.76$, $p = 3.51 \times 10^{-34}$, 95% CI 0.69–0.82) and layer 5 (rho $= -0.80$, $p = 1.01 \times 10^{-39}$, 95% CI −0.85 to −0.74), but not layer 6 (rho $= 0.086$, $p = 1.26$, 95% CI −0.07 to 0.23;

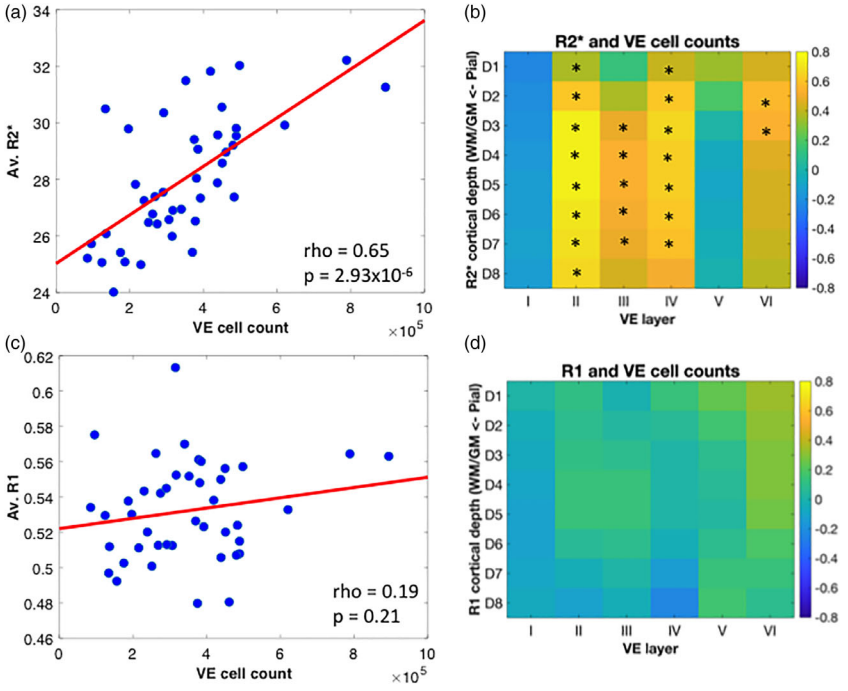

FIGURE 3 Relationship between R2*, R1 and von Economo cell count. (a) Average R2* against von Economo (VE) cell count for each VE MRI region of interest (ROI). Each blue dot is an ROI, were the *y*-axis represents the average R2*, for each ROI across participants, and the *x*-axis represents the average VE cell count, the red line represents a least squares linear regression line. (b) R2* across cortical depths against von Economo cortical layer cell count, where the *y*-axis represents R2* for each equi-volume cortical depth 1–8 and the *x*-axis represents VE cell number for each cortical layer I-VI, the colours represent the correlations across VE ROIs for R2* and VE cell count (highest—yellow, lowest—blue). (c) Average R1 against von Economo (VE) cell count for each VE MRI region of interest (ROI). (d) R1 across cortical depths against von Economo cortical layer cell count. Asterisks indicate Bonferroni-corrected significant correlations

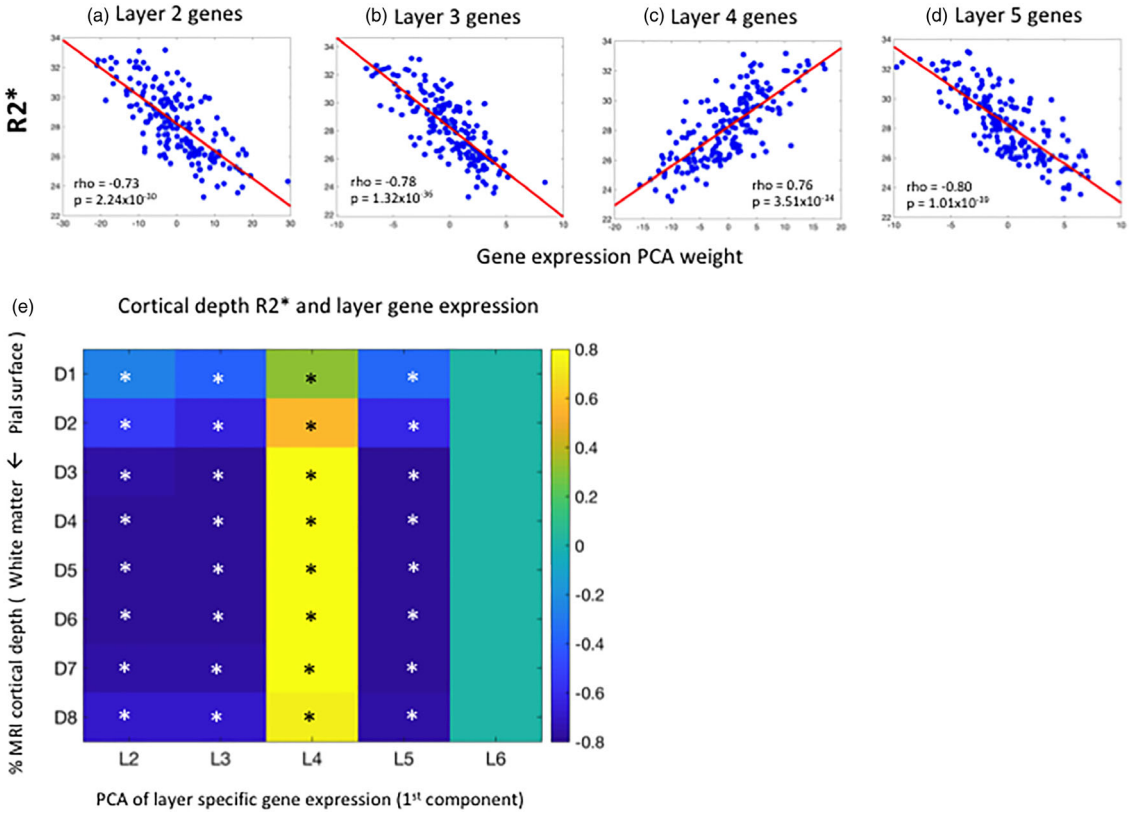

FIGURE 4 7T MRI R2* and cortical layer-specific genes. R2* against (a) layer 2 genes, (b) layer 3 genes, (c) layer 4 genes, (d) layer 5 genes. Each blue dot represents an ROI from the HCP-MMP 1.0 atlas, the *y*-axis represents R2*, averaged across participants, and the *x*-axis represents the PCA score for each ROI from the first PCA component of layer-specific gene expression. (e) R2* across cortical depths, where the *y*-axis represents R2* for each equi-volume cortical depth 1–8 and the *x*-axis represents the PCA score for each ROI from the first PCA component of layer-specific gene expression for layers II–VI, the colours represent the correlations across HCP-MMP 1.0 ROIs for R2* and layer-specific gene expression (most positive—yellow, most negative—blue). Asterisks indicate Bonferroni-corrected significant correlations

Figure 4a–d). Similarly, significant correlations were seen for R2* across cortical depths (averaged across ROIs) and genes specific for layers 2, 3, 4 and 5, but not for layer 6 (Figure 4e). Significant correlations for both PCA and mean gene expression analyses were in the same direction. No correlations between ROI averaged R1 and layer-specific genes were significant ($p > .2$, uncorrected for all correlations). In order to assess whether specific genes were driving the correlations with R2*, for each individual gene in the layer-specific gene lists correlations were performed between gene expression and ROI averaged R2*. This did not identify a single gene or group of genes that were driving these results (see Table S1). Cross-correlations of the PCA score of the first component for each set of layer-specific genes were observed, particularly for layers 2, 3 and 5 (see Supporting Information).

3.4 | R1 and R2* across cortical depths are highly correlated with R1/R2*-weighted white matter connections determined by DWI

The last step in our assessment examined the relationship between cortical depth dependent qMRI parameters and white matter connections estimated by DWI-based tractography. We hypothesised that UHF qMRI parameters across all cortical depths would correlate with characteristics of the cortico-cortical connections, as these project across cortical layers 2–6, while qMRI parameters near the GM/WM boundary would correlate with characteristics of cortico-striatal and cortico-thalamic connections as these project to the deep cortical layers 5 and 6.

For this analysis, whole brain diffusion tractography was performed in the same participants. A white matter connectome was generated and connections were then sub-divided into cortico-striatal (C-S), cortico-thalamic (C-T) and cortico-cortical (C-C). C-C connections were further sub-divided into inter-hemispheric (inter-H) and intra-hemispheric (intra-H), as inter-H connections are more vulnerable than intra-H connections in a number of neurodegenerative diseases (Lanskey et al., 2018; McColgan et al., 2017; Qiu et al., 2016). Following a tractometry approach, streamlines were either multiplied by: cross-sectional area (Smith et al., 2015) based on diffusion signal (streamline weighting); average R1 (R1 weighting); average R2* (R2* weighting). This type of tractometry is analogous to fractional anisotropy weighting performed in previous connectome studies (van den Heuvel & Sporns, 2011). Correlations were then performed for streamline-weighted connection subtypes against both R1 and R2* across cortical depths. White matter connections weighted by R1 and R2* were also correlated with R1 and R2*, respectively, across cortical depths.

The streamline-weighted connectome was not significantly correlated with either R1 or R2* across all cortical depths after Bonferroni correction (Figure 5a,b). However, the R1-weighted connectome showed Bonferroni corrected significance with R1 across nearly all cortical depths for cortico-striatal (depths 2–8), particularly at the GM/WM boundary, and intra-hemispheric connections (depths 2–3 and 7–8) (Figure 5c). Similarly the R2*-weighted connectome showed Bonferroni-corrected significance with R2* across nearly all cortical depths for cortico-striatal (depths 1–7) and intra-hemispheric (depths 1–8) white matter connections. Significant correlations were also seen for cortico-thalamic connections at superficial depths (depths 1–2) (Figure 5d).

4 | DISCUSSION

The aim of this study was to examine the potential and limitations of 7T qMRI measures across cortical depths by comparing cortical depth MPM measures for a 7T 500 μm whole brain acquisition to layer-specific cell histology and layer-specific gene expression and white matter connections derived from high-fidelity diffusion tractography. We show that R2* at different cortical depths strongly correlates with layer-specific cell count and layer-specific genes. Both, cortical grey matter R2* and R1 have strong correlations with cortical-striatal and intra-hemispheric R1 and R2*-weighted white matter connections. Correlations for all analyses were largely seen across cortical depths. The low layer-specificity may be related to high correlations of cell counts and gene expression across cortical layers. Our findings highlight the potential and limitations of cortical depth qMRI parameters as biomarkers for tracking the progression of neurodegenerative diseases with layer-specific vulnerability.

We first demonstrated that myelination profiles for the 7T MPMs presented here are consistent with post-mortem histology and previous 7T and 3T studies using R1 (Haast et al., 2016; Sereno et al., 2013), R2* (Marques et al., 2017) and T1w/T2w ratios (Glasser et al., 2016) as myelin markers. R2* across cortical depths is highly correlated with layer-specific cell counts from the von Economo atlas, indicating the sensitivity of R2* to layer-specific cytoarchitectonics. A one-to-one relationship of UHF qMRI and post-mortem histology, whereby UHF qMRI parameters at the pial surface would show high correlation with cells in superficial cortical layers and qMRI parameters at the GM/WM boundary would show correlation with cells in the deep layers, however was not demonstrated. The reason for this is at least in part related to high correlations of cell counts and cell staining across cortical layers (see Supporting Information). Given the high correlation across layers for post-mortem histology atlases, it is difficult to determine with this data alone the exact layer-specificity of qMRI.

In comparing 7T qMRI correlations with von Economo cell count a clear pattern emerges such that R2* shows higher correlations than R1 with post-mortem histological atlases. The relation between cytoarchitecture and the R2* and R1 parameters is believed to be largely mediated by the dependence of myeloarchitecture on cytoarchitecture (Dinse et al., 2015; Hellwig, 1993), since myeloarchitecture is known to influence macromolecular concentration and iron concentration as major MRI contrast drivers (Kirilina et al., 2020). The increased correlations of R2* over R1 with cytoarchitecture may be due to the co-localisation of iron and myelin typical in cortical regions (Fukunaga et al., 2010) leading to an additive effect for the

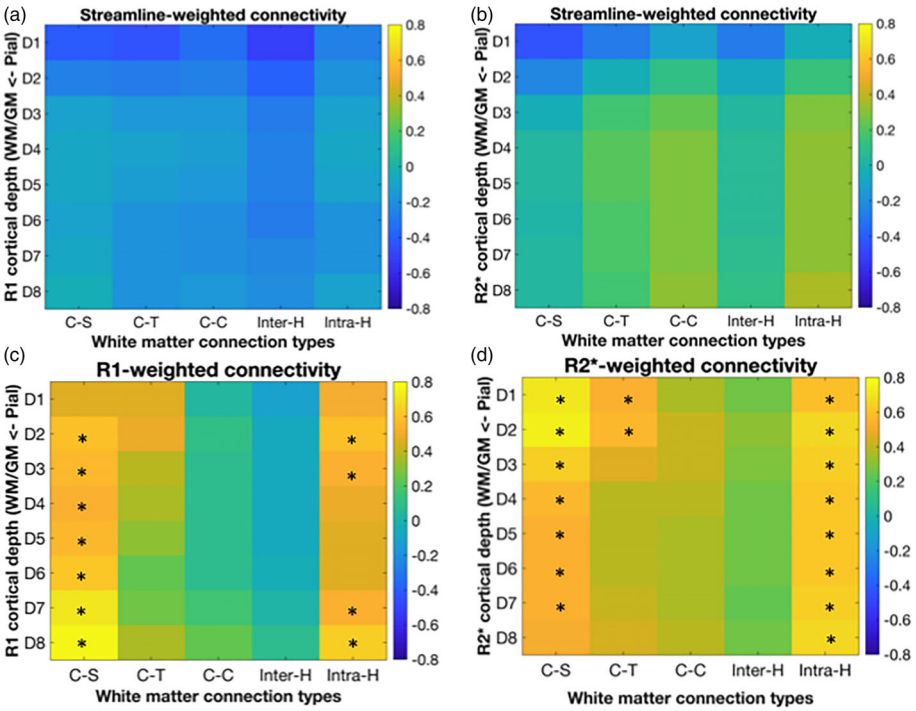

FIGURE 5 Cortical depth 7T qMRI is related to white matter connection subtypes. (a) R1 cortical depth against streamline-weighted connections, where the *y*-axis represents R1 across cortical depths averaged across participants and the *x*-axis represents streamline weighted connectivity for different white matter connection subtypes (cortical-striatal (C-S), cortical-thalamic (C-T), cortical-cortical (C-C), Inter-hemispheric (Inter-H), Intra-hemispheric (Intra-H), averaged across participants. Colours represent correlation across Desikan-Killiany atlas ROIs for R1 and streamline weighted connectivity (highest—yellow, lowest—blue), (b) R2* cortical depth against streamline-weighted connections, (c) R1 cortical depth against R1-weighted connections, (d) R2* cortical depth against R2*-weighted connections. Asterisks indicate Bonferroni-corrected significant correlations

myelination contrast particularly in R2* (Callaghan, Helms, Lutti, Mohammadi, & Weiskopf, 2015; Stuber et al., 2014). The correlation with cell number/cell staining intensity and R2* may thus reflect the iron present in both oligodendrocytes and neurons (Kirilina et al., 2020; Ward, Zucca, Duyn, Crichton, & Zecca, 2014) and macromolecules in myelin, whereas lower correlations are seen with R1 as this is mainly sensitive to macromolecules in myelin in oligodendrocytes, but much less so to the iron (Stuber et al., 2014).

This is supported by a recent study that used weighted gene co-expression network analysis (WGCNA) to understand the cellular composition underlying the R2t* component of R2*. The R2t* relaxation rate constant is sensitised to the cellular environment of water molecules. Using the AHBA the authors showed that R2t* was related to the regional expression of neurons and glia, including astrocytes, microglia and oligodendrocyte precursor cells (Wen, Goyal, Astafiev, Raichle, & Yablonskiy, 2018).

The increased contrast and sensitivity may make R2* a more reliable measure of myelination at 7T, since the contrast in R2* driven by microstructural iron is increasing with field strength in addition to the overall SNR increase due to the higher field. This was further indicated by cortical profiles in the middle temporal area and superior parietal cortex where R1 and R2* cortical profiles diverged, such that R2* was more reflective of patterns seen in (Glasser et al., 2016).

Consistently, a higher sensitivity of R2* compared to R1 was also found for the gene expression analysis. For cortical layer-specific genes significant correlations are seen for layers 2, 3, 4 and 5 and R2*. For layers 2, 3 and 5 correlations with R2* were negative, whereas correlation with layer 4 was positive. This is in keeping with a study at 3T examining gene expression at different cortical levels using the T1w/T2w ratio (Burt et al., 2018). In Burt et al. layer-specific gene lists were obtained from a study analysing the visual and mid-temporal cortex of post-mortem adult brains, where genes were assigned to cortical layers (Zeng et al., 2012). For our study we replicated these findings using a more extensive layer-specific gene list obtained from a study of 10 distinct cortical regions in the macaque (Bernard et al., 2012). The previously reported negative correlations between T1w/T2w ratios with layers 1–3 and positive correlations with layer 4 genes have been interpreted in the context of the thick and well-defined granular layer 4 in primary sensory areas in contrast to a gradual loss of the granular layer in association cortices with progression up hierarchical levels (Burt et al., 2018). During cortical development there is a complex interplay between genes driving layer-specific development, such that genes associated with development of superficial layers suppress those involved in development of deep layers and vice versa (Greig, Woodworth, Galazo, Padmanabhan, & Macklis, 2013). While this does not explain the R2* negative correlation with layer 2, 3 and 5 specific genes and positive correlation with layer 4 genes we observed, the interplay between layer-specific genes may be a contributing factor. We note that correlations with layer-specific gene expression were again found across multiple cortical depths. This may be partly explained by the high cross-correlations between layer-specific genes (Figures 4 and Figure S2c) obfuscating the layer specificity of qMRI measures.

To link cortical grey matter and white matter connections, that is, the connectome, we tested correlations between specific (R1 and R2* weighted) white matter connections with R1 and R2* across cortical depths. Significant correlations were seen for both R1 and R2* with cortico-striatal and intra-hemispheric white matter connections. For R1 the strongest correlations for cortico-striatal connections were seen at the lowest cortical depths, consistent with pyramidal tract

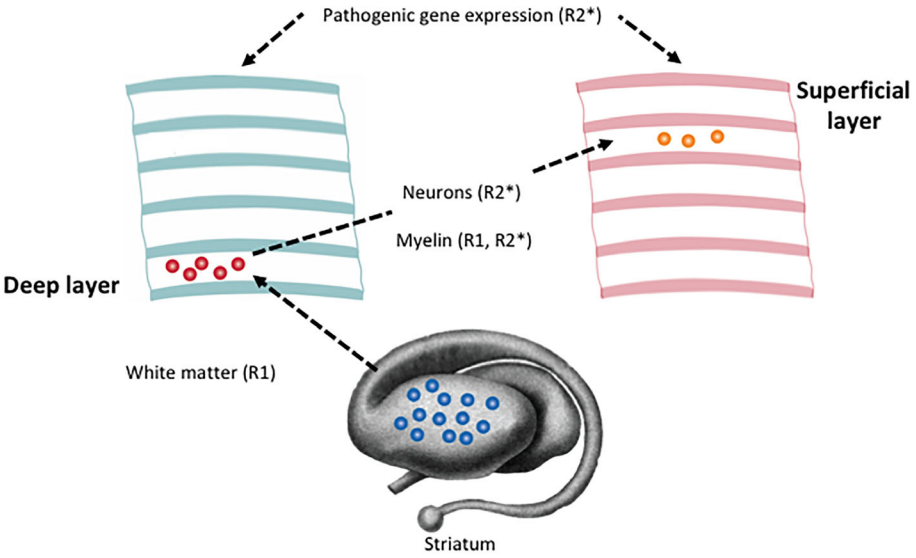

FIGURE 6 A high anatomical precision framework for neurodegenerative disease. Schematic showing how we can use qMRI and the relationships identified in this study to combine information on white matter (R1, R2*), neuronal count across cortical depths (R2*), myelination across cortical depths (R1, R2*) and pathogenic gene expression (R2*) to provide a comprehensive picture of neurodegeneration

neurons in layer 5 forming ipsilateral connections with the striatum (Shepherd, 2013), while intra-hemispheric connections showed correlations across all cortical depths for R2*, consistent with intra-telencephalic pyramidal neurons present in layers 2–6 forming cortico-cortical connections (Molyneaux, Arlotta, Menezes, & Macklis, 2007). Correlations between R2* and cortico-striatal connections were highest at superficial depths, however this may be related to the directional dependence of R2* in white matter due to microstructure orientation and myelin concentration (Rudko et al., 2014). No significant correlations were seen for streamline weighted connections, this suggests that there is a stronger relationship with R1/R2* in white matter and cortical grey matter than inter-modal comparisons using diffusion MRI based streamline weighting in white matter and qMRI (R1/R2*) measures in grey matter.

A previous study has shown that Big Brain cell staining intensities across cortical depths are strongly correlated with intra-hemispheric white matter connections between cortical regions (Wei, Scholtens, Turk, & van den Heuvel, 2019). This is in keeping with our results showing high correlations between intra-hemispheric connections and R1 and R2* across cortical depths.

In this study, we have shown that R2* at different cortical depths strongly correlates with layer-specific cell count, cell staining intensity and layer-specific genes. Furthermore, both cortical grey matter R2* and R1 have strong correlations with cortical-striatal and intra-hemispheric R1 and R2*-weighted white matter connections. We note that these correlations typically spread across multiple cortical depths for the qMRI measures. This can be partly explained by high correlations across layers we observed for cytoarchitectonics and gene expression data. Limited spatial sampling density and consequent partial volume effects at the qMRI resolution of 500 μm compared to typically smaller thickness of anatomical layers, as discussed by (Dinse et al., 2015), most likely further contributed to the lack of layer specificity. Challenges of precise registration, segmentation and MRI-based depth/layer definition may add further to spatial imprecisions and reduce the effective spatial resolution (Bazin et al., 2014; Trampel et al., 2019).

Despite the limited specificity of qMRI layer measures this study demonstrates their sensitivity to and connection to neurobiologically relevant cytoarchitecture, gene expression and white matter connections. This suggests that the metrics can be used to build an anatomical framework that could be used to track plasticity and pathology more precisely compared to previous approaches that ignored layer differences. Particularly, the origin and the spread of neurodegeneration may be mapped. For example, Huntington's disease causes striatal atrophy (Tabrizi et al., 2009) and loss of cortico-striatal white matter connections (McColgan et al., 2015; McColgan et al., 2017) prior to symptom onset, with subsequent cell death in cortical layers 3, 5 and 6 during the end stages of disease (Rub et al., 2016). Track disease progression with the proposed framework, we expect that deep cortical layers will be affected first, in keeping with the early loss of cortico-striatal connections, followed by superficial layers and that the inter-regional patterns of cortical degeneration will be associated with the regional expression of HD related genes (Figure 6). Thus, the combination of 7T MPMs, white matter connections and pathogenic gene expression can be used to form a comprehensive picture of the mechanism of neurodegeneration, going beyond conventional non-invasive approaches.

ACKNOWLEDGEMENTS

We would like to thank Dr. Evgeniya Kirilina for her advice regarding study design. We would also like to thank the University of Minnesota Center for Magnetic Resonance Research for the provision of the multiband EPI sequence software. We would like to thank C. Rüger and R. Haak (Department of Cardiology, Endodontology and Periodontology, University Medical Center Leipzig) for manufacturing the mouth guards for the optical prospective motion correction. The research leading to these results has received funding from the European Research Council under the European Union's Seventh

Framework Programme (FP7/2007-2013)/ERC grant agreement n° 616905. N.W. received funding from the BMBF (01EW1711A & B) in the framework of ERA-NET NEURON, and from the NISCI project funded by the European Union's Horizon 2020 research and innovation programme under the grant agreement No 681094, and the Swiss State Secretariat for Education, Research and Innovation (SERI) under contract number 15.0137. Open access funding enabled and organized by Projekt DEAL.

CONFLICT OF INTEREST

The Max Planck Institute for Human Cognitive and Brain Sciences and Wellcome Centre for Human Neuroimaging have institutional research agreements with Siemens Healthcare. N.W. holds a patent on acquisition of MRI data during spoiler gradients (US 10,401,453 B2). N.W. was a speaker at an event organised by Siemens Healthcare and was reimbursed for the travel expenses.

DATA AVAILABILITY STATEMENT

FreeSurfer files of group-averaged cortical surface data are available to allow the replication of Figure 1. For Figures 2–5 and Table S1 all data and code is available. Please see https://gitlab.gwdg.de/pmccolgan/7t_layers and source_data_readme.txt for a complete description of the data. We are unable to share raw MRI images due to data protection restrictions.

ETHICS STATEMENT

Ten right-handed healthy volunteers with no history of neurological disorders participated in the study after giving informed written consent. The experimental procedures had been previously approved by the Ethics Committee at the Medical Faculty of the University of Leipzig (Reg.-No. 273-14-25082014).

REFERENCES

Andersson, J. L., & Sotiropoulos, S. N. (2016). An integrated approach to correction for off-resonance effects and subject movement in diffusion MR imaging. *NeuroImage*, *125*, 1063–1078. https://doi.org/10.1016/j.neuroimage.2015.10.019

Arnatkevic Iute, A., Fulcher, B. D., & Fornito, A. (2019). A practical guide to linking brain-wide gene expression and neuroimaging data. *NeuroImage*, *189*, 353–367. https://doi.org/10.1016/j.neuroimage.2019.01.011

Bazin, P. L., Weiss, M., Dinse, J., Schafer, A., Trampel, R., & Turner, R. (2014). A computational framework for ultra-high resolution cortical segmentation at 7Tesla. *NeuroImage*, *93*(Pt 2), 201–209. https://doi.org/10.1016/j.neuroimage.2013.03.077

Bernard, A., Lubbers, L. S., Tanis, K. Q., Luo, R., Podtelezhnikov, A. A., Finney, E. M., … Lein, E. S. (2012). Transcriptional architecture of the primate neocortex. *Neuron*, *73*(6), 1083–1099. https://doi.org/10.1016/j.neuron.2012.03.002

Burt, J. B., Demirtas, M., Eckner, W. J., Navejar, N. M., Ji, J. L., Martin, W. J., … Murray, J. D. (2018). Hierarchy of transcriptomic specialization across human cortex captured by structural neuroimaging topography. *Nature Neuroscience*, *21*(9), 1251–1259. https://doi.org/10.1038/s41593-018-0195-0

Callaghan, M. F., Helms, G., Lutti, A., Mohammadi, S., & Weiskopf, N. (2015). A general linear relaxometry model of R1 using imaging data. *Magnetic Resonance in Medicine*, *73*(3), 1309–1314. https://doi.org/10.1002/mrm.25210

Callaghan, M. F., Josephs, O., Herbst, M., Zaitsev, M., Todd, N., & Weiskopf, N. (2015). An evaluation of prospective motion correction (PMC) for high resolution quantitative MRI. *Frontiers in Neuroscience*, *9*, 97. https://doi.org/10.3389/fnins.2015.00097

Carey, D., Caprini, F., Allen, M., Lutti, A., Weiskopf, N., Rees, G., … Dick, F. (2018). Quantitative MRI provides markers of intra-, inter-regional, and age-related differences in young adult cortical microstructure. *NeuroImage*, *182*, 429–440. https://doi.org/10.1016/j.neuroimage.2017.11.066

Cohen-Adad, J., Polimeni, J. R., Helmer, K. G., Benner, T., McNab, J. A., Wald, L. L., … Mainero, C. (2012). T(2)* mapping and B(0) orientation-dependence at 7 T reveal cyto- and myeloarchitecture organization of the human cortex. *NeuroImage*, *60*(2), 1006–1014. https://doi.org/10.1016/j.neuroimage.2012.01.053

Derakhshan, M., Caramanos, Z., Narayanan, S., Arnold, D. L., & Louis Collins, D. (2014). Surface-based analysis reveals regions of reduced cortical magnetization transfer ratio in patients with multiple sclerosis: A proposed method for imaging subpial demyelination. *Human Brain Mapping*, *35*(7), 3402–3413. https://doi.org/10.1002/hbm.22410

Desikan, R. S., Segonne, F., Fischl, B., Quinn, B. T., Dickerson, B. C., Blacker, D., … Killiany, R. J. (2006). An automated labeling system for subdividing the human cerebral cortex on MRI scans into gyral based regions of interest. *NeuroImage*, *31*(3), 968–980. https://doi.org/10.1016/j.neuroimage.2006.01.021

Dick, F., Tierney, A. T., Lutti, A., Josephs, O., Sereno, M. I., & Weiskopf, N. (2012). In vivo functional and myeloarchitectonic mapping of human primary auditory areas. *The Journal of Neuroscience*, *32*(46), 16095–16105. https://doi.org/10.1523/JNEUROSCI.1712-12.2012

Dinse, J., Hartwich, N., Waehnert, M. D., Tardif, C. L., Schafer, A., Geyer, S., … Bazin, P. L. (2015). A cytoarchitecture-driven myelin model reveals area-specific signatures in human primary and secondary areas using ultra-high resolution in-vivo brain MRI. *NeuroImage*, *114*, 71–87. https://doi.org/10.1016/j.neuroimage.2015.04.023

Edwards, L. J., Kirilina, E., Mohammadi, S., & Weiskopf, N. (2018). Microstructural imaging of human neocortex in vivo. *NeuroImage*, *182*, 184–206. https://doi.org/10.1016/j.neuroimage.2018.02.055

Farokhian, F., Beheshti, I., Sone, D., & Matsuda, H. (2017). Comparing CAT12 and VBM8 for detecting brain morphological abnormalities in temporal lobe epilepsy. *Frontiers in Neurology*, *8*, 428. https://doi.org/10.3389/fneur.2017.00428

Feinberg, D. A., Moeller, S., Smith, S. M., Auerbach, E., Ramanna, S., Gunther, M., … Yacoub, E. (2010). Multiplexed echo planar imaging for sub-second whole brain FMRI and fast diffusion imaging. *PLoS One*, *5*(12), e15710. https://doi.org/10.1371/journal.pone.0015710

Fischl, B., van der Kouwe, A., Destrieux, C., Halgren, E., Segonne, F., Salat, D. H., … Dale, A. M. (2004). Automatically parcellating the human cerebral cortex. *Cerebral Cortex*, *14*(1), 11–22.

Fukunaga, M., Li, T. Q., van Gelderen, P., de Zwart, J. A., Shmueli, K., Yao, B., … Duyn, J. H. (2010). Layer-specific variation of iron content in cerebral cortex as a source of MRI contrast. *Proceedings of the National Academy of Sciences of the United States of America*, *107*(8), 3834–3839. https://doi.org/10.1073/pnas.0911177107

Geyer, S., Ledberg, A., Schleicher, A., Kinomura, S., Schormann, T., Burgel, U., … Roland, P. E. (1996). Two different areas within the primary motor cortex of man. *Nature*, *382*(6594), 805–807. https://doi.org/10.1038/382805a0

Glasser, M. F., Coalson, T. S., Robinson, E. C., Hacker, C. D., Harwell, J., Yacoub, E., … Van Essen, D. C. (2016). A multi-modal parcellation of human cerebral cortex. *Nature*, *536*, 171–178. https://doi.org/10.1038/nature18933

Greig, L. C., Woodworth, M. B., Galazo, M. J., Padmanabhan, H., & Macklis, J. D. (2013). Molecular logic of neocortical projection neuron specification, development and diversity. *Nature Reviews. Neuroscience*, *14*(11), 755–769. https://doi.org/10.1038/nrn3586

Griswold, M. A., Jakob, P. M., Heidemann, R. M., Nittka, M., Jellus, V., Wang, J., … Haase, A. (2002). Generalized autocalibrating partially parallel acquisitions (GRAPPA). *Magnetic Resonance in Medicine*, *47*(6), 1202–1210. https://doi.org/10.1002/mrm.10171

Haast, R. A., Ivanov, D., Formisano, E., & Uludag, K. (2016). Reproducibility and reliability of quantitative and weighted T1 and T2(*) mapping for myelin-based cortical Parcellation at 7 tesla. *Frontiers in Neuroanatomy*, *10*, 112. https://doi.org/10.3389/fnana.2016.00112

Hawrylycz, M. J., Lein, E. S., Guillozet-Bongaarts, A. L., Shen, E. H., Ng, L., Miller, J. A., … Jones, A. R. (2012). An anatomically comprehensive atlas of the adult human brain transcriptome. *Nature*, *489*(7416), 391–399. https://doi.org/10.1038/nature11405

Hellwig, B. (1993). How the myelin picture of the human cerebral cortex can be computed from cytoarchitectural data. A bridge between von Economo and Vogt. *Journal für Hirnforschung*, *34*(3), 387–402.

Hopf, A. (1968). Registration of the myeloarchitecture of the human frontal lobe with an extinction method. *Journal für Hirnforschung*, *10*(3), 259–269.

Huntenburg, J. M., Steele, C. J., & Bazin, P. L. (2018). Nighres: Processing tools for high-resolution neuroimaging. *Gigascience*, *7*(7), 1–9. https://doi.org/10.1093/gigascience/giy082

Jeurissen, B., Tournier, J. D., Dhollander, T., Connelly, A., & Sijbers, J. (2014). Multi-tissue constrained spherical deconvolution for improved analysis of multi-shell diffusion MRI data. *NeuroImage*, *103*, 411–426. https://doi.org/10.1016/j.neuroimage.2014.07.061

Kellner, E., Dhital, B., Kiselev, V. G., & Reisert, M. (2016). Gibbs-ringing artifact removal based on local subvoxel-shifts. *Magnetic Resonance in Medicine*, *76*(5), 1574–1581. https://doi.org/10.1002/mrm.26054

Kirilina, E., Helbling, S., Morawski, M., Pine, K., Reimann, K., Jankuhn, S., … Weiskopf, N. (2020). Superficial white matter imaging: Contrast mechanisms and whole-brain in vivo mapping. *Science Advances*, *6*(41), eaaz9281. https://doi.org/10.1126/sciadv.aaz9281

Lanskey, J. H., McColgan, P., Schrag, A. E., Acosta-Cabronero, J., Rees, G., Morris, H. R., & Weil, R. S. (2018). Can neuroimaging predict dementia in Parkinson's disease? *Brain*, *141*(9), 2545–2560. https://doi.org/10.1093/brain/awy211

Lutti, A., Dick, F., Sereno, M. I., & Weiskopf, N. (2014). Using high-resolution quantitative mapping of R1 as an index of cortical myelination. *NeuroImage*, *93*(Pt 2), 176–188. https://doi.org/10.1016/j.neuroimage.2013.06.005

Maggioni, M., Katkovnik, V., Egiazarian, K., & Foi, A. (2013). Nonlocal transform-domain filter for volumetric data denoising and reconstruction. *IEEE Transactions on Image Processing*, *22*(1), 119–133. https://doi.org/10.1109/TIP.2012.2210725

Marques, J. P., Khabipova, D., & Gruetter, R. (2017). Studying cyto and myeloarchitecture of the human cortex at ultra-high field with quantitative imaging: R1, R2(*) and magnetic susceptibility. *NeuroImage*, *147*, 152–163. https://doi.org/10.1016/j.neuroimage.2016.12.009

McColgan, P., Seunarine, K. K., Gregory, S., Razi, A., Papoutsi, M., Long, J. D., … Investigators, T. T. H. (2017). Topological length of white matter connections predicts their rate of atrophy in premanifest Huntington's disease. *JCI Insight*, *2*(8), 1–16. https://doi.org/10.1172/jci.insight.92641

McColgan, P., Seunarine, K. K., Razi, A., Cole, J. H., Gregory, S., Durr, A., … Track, H. D. I. (2015). Selective vulnerability of Rich Club brain regions is an organizational principle of structural connectivity loss in Huntington's disease. *Brain*, *138*(Pt 11), 3327–3344. https://doi.org/10.1093/brain/awv259

Moeller, S., Yacoub, E., Olman, C. A., Auerbach, E., Strupp, J., Harel, N., & Ugurbil, K. (2010). Multiband multislice GE-EPI at 7 tesla, with 16-fold acceleration using partial parallel imaging with application to high spatial and temporal whole-brain fMRI. *Magnetic Resonance in Medicine*, *63*(5), 1144–1153. https://doi.org/10.1002/mrm.22361

Molyneaux, B. J., Arlotta, P., Menezes, J. R., & Macklis, J. D. (2007). Neuronal subtype specification in the cerebral cortex. *Nature Reviews. Neuroscience*, *8*(6), 427–437. https://doi.org/10.1038/nrn2151

Nagy, Z., & Weiskopf, N. (2008). Efficient fat suppression by slice-selection gradient reversal in twice-refocused diffusion encoding. *Magnetic Resonance in Medicine*, *60*(5), 1256–1260. https://doi.org/10.1002/mrm.21746

Papoutsi, M., Magerkurth, J., Josephs, O., Pépés, S. E., Ibitoye, T., Reilmann, R., … Tabrizi, S. J. (2018). Activity-is better than connectivity-neurofeedback training in Huntington's disease. *bioRxiv*, 481903. https://doi.org/10.1101/481903

Qiu, Y., Liu, S., Hilal, S., Loke, Y. M., Ikram, M. K., Xu, X., … Zhou, J. (2016). Inter-hemispheric functional dysconnectivity mediates the association of corpus callosum degeneration with memory impairment in AD and amnestic MCI. *Scientific Reports*, *6*, 32573. https://doi.org/10.1038/srep32573

Rub, U., Seidel, K., Heinsen, H., Vonsattel, J. P., den Dunnen, W. F., & Korf, H. W. (2016). Huntington's disease (HD): The neuropathology of a multisystem neurodegenerative disorder of the human brain. *Brain Pathology*, *26*(6), 726–740. https://doi.org/10.1111/bpa.12426

Rudko, D. A., Klassen, L. M., de Chickera, S. N., Gati, J. S., Dekaban, G. A., & Menon, R. S. (2014). Origins of R2* orientation dependence in gray and white matter. *Proceedings of the National Academy of Sciences of the United States of America*, *111*(1), E159-167. doi:https://doi.org/10.1073/pnas.1306516111

Scholtens, L. H., de Reus, M. A., de Lange, S. C., Schmidt, R., & van den Heuvel, M. P. (2018). An MRI Von Economo—Koskinas atlas. *NeuroImage*, *170*, 249–256. https://doi.org/10.1016/j.neuroimage.2016.12.069

Scholtens, L. H., de Reus, M. A., & van den Heuvel, M. P. (2015). Linking contemporary high resolution magnetic resonance imaging to the von Economo legacy: A study on the comparison of MRI cortical thickness and histological measurements of cortical structure. *Human Brain Mapping*, *36*(8), 3038–3046. https://doi.org/10.1002/hbm.22826

Sereno, M. I., Lutti, A., Weiskopf, N., & Dick, F. (2013). Mapping the human cortical surface by combining quantitative T(1) with retinotopy. *Cerebral Cortex*, *23*(9), 2261–2268. https://doi.org/10.1093/cercor/bhs213

Setsompop, K., Gagoski, B. A., Polimeni, J. R., Witzel, T., Wedeen, V. J., & Wald, L. L. (2012). Blipped-controlled aliasing in parallel imaging for simultaneous multislice echo planar imaging with reduced g-factor penalty. *Magnetic Resonance in Medicine*, *67*(5), 1210–1224. https://doi.org/10.1002/mrm.23097

Shepherd, G. M. (2013). Corticostriatal connectivity and its role in disease. *Nature Reviews. Neuroscience*, *14*(4), 278–291. https://doi.org/10.1038/nrn3469

Smith, R. E., Tournier, J. D., Calamante, F., & Connelly, A. (2012). Anatomically-constrained tractography: Improved diffusion MRI streamlines tractography through effective use of anatomical information. *NeuroImage*, *62*(3), 1924–1938. https://doi.org/10.1016/j.neuroimage.2012.06.005

Smith, R. E., Tournier, J. D., Calamante, F., & Connelly, A. (2013). SIFT: Spherical-deconvolution informed filtering of tractograms. *NeuroImage*, *67*, 298–312. https://doi.org/10.1016/j.neuroimage.2012.11.049

Smith, R. E., Tournier, J. D., Calamante, F., & Connelly, A. (2015). SIFT2: Enabling dense quantitative assessment of brain white matter connectivity using streamlines tractography. *NeuroImage*, *119*, 338–351. https://doi.org/10.1016/j.neuroimage.2015.06.092

Sprooten, E., O'Halloran, R., Dinse, J., Lee, W. H., Moser, D. A., Doucet, G. E., … Frangou, S. (2019). Depth-dependent intracortical myelin organization in the living human brain determined by in vivo ultra-high field magnetic resonance imaging. *NeuroImage*, *185*, 27–34. https://doi.org/10.1016/j.neuroimage.2018.10.023

Stuber, C., Morawski, M., Schafer, A., Labadie, C., Wahnert, M., Leuze, C., … Turner, R. (2014). Myelin and iron concentration in the human brain: A quantitative study of MRI contrast. *NeuroImage*, *93*(Pt 1), 95–106. https://doi.org/10.1016/j.neuroimage.2014.02.026

Tabelow, K., Balteau, E., Ashburner, J., Callaghan, M. F., Draganski, B., Helms, G., … Mohammadi, S. (2019). hMRI—A toolbox for quantitative MRI in neuroscience and clinical research. *NeuroImage*, *194*, 191–210. https://doi.org/10.1016/j.neuroimage.2019.01.029

Tabrizi, S. J., Langbehn, D. R., Leavitt, B. R., Roos, R. A., Durr, A., Craufurd, D., … Stout, J. C. (2009). Biological and clinical manifestations of Huntington's disease in the longitudinal TRACK-HD study: Cross-sectional analysis of baseline data. *Lancet Neurology*, *8*(9), 791–801. https://doi.org/10.1016/S1474-4422(09)70170-X

Tardif, C. L., Bedell, B. J., Eskildsen, S. F., Collins, D. L., & Pike, G. B. (2012). Quantitative magnetic resonance imaging of cortical multiple sclerosis pathology. *Multiple Sclerosis International*, *2012*, 742018. https://doi.org/10.1155/2012/742018

Tournier, J. D., Calamante, F., & Connelly, A. (2012). MRtrix: Diffusion tractography in crossing fiber regions. *Imaging Systems and Technology*, *22*(1), 53–56.

Trampel, R., Bazin, P. L., Pine, K., & Weiskopf, N. (2019). In-vivo magnetic resonance imaging (MRI) of laminae in the human cortex. *NeuroImage*, *197*, 707–715. https://doi.org/10.1016/j.neuroimage.2017.09.037

Tustison, N. J., Avants, B. B., Cook, P. A., Zheng, Y., Egan, A., Yushkevich, P. A., & Gee, J. C. (2010). N4ITK: Improved N3 bias correction. *IEEE Transactions on Medical Imaging*, *29*(6), 1310–1320. https://doi.org/10.1109/TMI.2010.2046908

van den Heuvel, M. P., Scholtens, L. H., & Kahn, R. S. (2019). Multiscale neuroscience of psychiatric disorders. *Biological Psychiatry*, *86*(7), 512–522. https://doi.org/10.1016/j.biopsych.2019.05.015

van den Heuvel, M. P., & Sporns, O. (2011). Rich-club organization of the human connectome. *The Journal of Neuroscience*, *31*(44), 15775–15786. https://doi.org/10.1523/JNEUROSCI.3539-11.2011

Veraart, J., Novikov, D. S., Christiaens, D., Ades-Aron, B., Sijbers, J., & Fieremans, E. (2016). Denoising of diffusion MRI using random matrix theory. *NeuroImage*, *142*, 394–406. https://doi.org/10.1016/j.neuroimage.2016.08.016

Vogt, C., & Vogt, O. (1919). Ergebnisse unserer hirnforschung. 1.-4. Mitteilung. *Journal of Psychology and Neurology*, *25*, 279–461.

von Economo, C. (2009). Cellular structure of the human cerebral cortex. In L. C. Triarhou (Ed.), *Translator*. Basel: Karger Medical and Scientific Publishers.

von Economo, C. F. K., & Koskinas, G. N. (1925). *Die cytoarchitektonik der hirnrinde des erwachsenen menschen*. Berlin: Springer.

Ward, R. J., Zucca, F. A., Duyn, J. H., Crichton, R. R., & Zecca, L. (2014). The role of iron in brain ageing and neurodegenerative disorders. *Lancet Neurology*, *13*(10), 1045–1060. https://doi.org/10.1016/S1474-4422(14)70117-6

Wei, Y., Scholtens, L. H., Turk, E., & van den Heuvel, M. P. (2019). Multiscale examination of cytoarchitectonic similarity and human brain connectivity. *Network Neuroscience*, *3*(1), 124–137. https://doi.org/10.1162/netn_a_00057

Weiskopf, N., Edwards, L. J., Helms, G., Mohammadi, S., & Kirilina, E. (2021). Quantitative magnetic resonance imaging of brain anatomy and in-vivo histology. *Nature Reviews Physics*.

Weiskopf, N., Lutti, A., Helms, G., Novak, M., Ashburner, J., & Hutton, C. (2011). Unified segmentation based correction of R1 brain maps for RF transmit field inhomogeneities (UNICORT). *NeuroImage*, *54*(3), 2116–2124. https://doi.org/10.1016/j.neuroimage.2010.10.023

Weiskopf, N., Mohammadi, S., Lutti, A., & Callaghan, M. F. (2015). Advances in MRI-based computational neuroanatomy: From morphometry to in-vivo histology. *Current Opinion in Neurology*, *28*(4), 313–322. https://doi.org/10.1097/WCO.0000000000000222

Weiskopf, N., Suckling, J., Williams, G., Correia, M. M., Inkster, B., Tait, R., … Lutti, A. (2013). Quantitative multi-parameter mapping of R1, PD(*), MT, and R2(*) at 3T: A multi-center validation. *Frontiers in Neuroscience*, *7*, 95. https://doi.org/10.3389/fnins.2013.00095

Wen, J., Goyal, M. S., Astafiev, S. V., Raichle, M. E., & Yablonskiy, D. A. (2018). Genetically defined cellular correlates of the baseline brain MRI signal. *Proceedings of the National Academy of Sciences of the United States of America*, *115*(41), E9727–E9736. https://doi.org/10.1073/pnas.1808121115

Xu, J., Moeller, S., Auerbach, E. J., Strupp, J., Smith, S. M., Feinberg, D. A., … Ugurbil, K. (2013). Evaluation of slice accelerations using multiband echo planar imaging at 3 T. *NeuroImage*, *83*, 991–1001. https://doi.org/10.1016/j.neuroimage.2013.07.055

Yeh, C. H., Smith, R. E., Liang, X., Calamante, F., & Connelly, A. (2018). Investigating the streamline count required for reproducible structural connectome construction across a range of brain parcellation resolutions. In *Paper presented at the ISMRM Paris, France*.

Zeng, H., Shen, E. H., Hohmann, J. G., Oh, S. W., Bernard, A., Royall, J. J., … Jones, A. R. (2012). Large-scale cellular-resolution gene profiling in human neocortex reveals species-specific molecular signatures. *Cell*, *149*(2), 483–496. https://doi.org/10.1016/j.cell.2012.02.052

Zilles, K., Palomero-Gallagher, N., & Amunts, K. (2015). Myeloarchitecture and maps of the cerebral cortex. In A. W. Toga (Ed.), *Brain mapping* (pp. 137–156). Waltham: Academic Press.

SUPPORTING INFORMATION

Additional supporting information may be found online in the Supporting Information section at the end of this article.

How to cite this article: McColgan, P., Helbling, S., Vaculčiaková, L., Pine, K., Wagstyl, K., Attar, F. M., Edwards, L., Papoutsi, M., Wei, Y., Van den Heuvel, M. P., Tabrizi, S. J., Rees, G., & Weiskopf, N. (2021). Relating quantitative 7T MRI across cortical depths to cytoarchitectonics, gene expression and connectomics. *Human Brain Mapping*, *42*(15), 4996–5009. https://doi.org/10.1002/hbm.25595